

## THE COSMIC BACKGROUND IMAGER

S. PADIN, M.C. SHEPHERD, J.K. CARTWRIGHT, R.G. KEENEY, B.S. MASON, T.J. PEARSON,  
A.C.S. READHEAD, W.L. SCHAALE, J. SIEVERS, P.S. UDOMPRASET AND J.K. YAMASAKI

California Institute of Technology, MS 105-24, Pasadena, CA 91125

spadin@caltech.edu, mcs@astro.caltech.edu, jkc@astro.caltech.edu, rgk@ovro.caltech.edu,  
bsm@astro.caltech.edu, tjp@astro.caltech.edu, acr@astro.caltech.edu, wschaal@aol.com, js@astro.caltech.edu,  
psu@astro.caltech.edu, jky@astro.caltech.edu

W.L. HOLZAPFEL

University of California, Department of Physics, 426 LeConte Hall, Berkeley, CA 94720  
swlh@cpfa.berkeley.edu

J.E. CARLSTROM

University of Chicago, Department of Astronomy and Astrophysics, 5640 S. Ellis Ave., Chicago, IL 60637;  
jc@hyde.uchicago.edu

M. JOY

NASA Marshall Space Flight Center, Dept. Space Science SD50, Huntsville, AL 35812  
marshall. joy@msfc.nasa.gov

S.T. MYERS

National Radio Astronomy Observatory, PO Box 0, Socorro NM 87801  
smyers@aoc.nrao.edu

AND

A. OTAROLA

European Southern Observatory, Balmaceda 2536, Antofagasta, Chile  
aotarola@eso.org

*Draft version February 1, 2008*

## ABSTRACT

Design and performance details are given for the Cosmic Background Imager (CBI), an interferometer array that is measuring the power spectrum of fluctuations in the cosmic microwave background radiation (CMBR) for multipoles in the range  $400 < l < 3500$ . The CBI is located at an altitude of 5000 m in the Atacama Desert in northern Chile. It is a planar synthesis array with 13 0.9-m diameter antennas on a 6-m diameter tracking platform. Each antenna has a cooled, low-noise receiver operating in the 26–36 GHz band. Signals are cross-correlated in an analog filterbank correlator with ten 1 GHz bands. This allows spectral index measurements which can be used to distinguish CMBR signals from diffuse galactic foregrounds. A 1.2 kHz 180° phase switching scheme is used to reject cross-talk and low-frequency pickup in the signal processing system. The CBI has a 3-axis mount which allows the tracking platform to be rotated about the optical axis, providing improved  $(u, v)$  coverage and a powerful discriminant against false signals generated in the receiving electronics. Rotating the tracking platform also permits polarization measurements when some of the antennas are configured for the orthogonal polarization.

*Subject headings:* instrumentation: interferometers —cosmic microwave background

## 1. INTRODUCTION

The cosmic microwave background radiation (CMBR) offers us a unique view of the early universe. Small-scale anisotropies in the CMBR contain information about acoustic oscillations in the primordial plasma and provide a way of measuring the fundamental cosmological parameters (Hu and White 1997; Hu et al. 1997). Anisotropies have been observed on angular scales from a few degrees to  $\sim \frac{1}{4}^\circ$  at the level of a few tens of  $\mu\text{K}$ , but measurements on smaller angular scales are important because they can be used to further constrain  $\Omega_b$ ,  $\Omega_\Lambda$ ,  $h$  and the slope of the primordial fluctuation spectrum. In this paper, we describe the Cosmic Background Imager (CBI), an interferometer array which is measuring CMBR anisotropies on angular scales in the range  $\sim 5' - 0.5^\circ$ .

The goal of CMBR anisotropy measurements is to measure the angular power spectrum of the sky intensity distribution,  $P_{sky}$ . On small angular scales, this is the Fourier Transform (FT) of the sky temperature autocorrelation function,  $C_{sky}$ . A radio telescope measures the convolution

of the sky brightness,  $I_{sky}$ , with the telescope beam pattern,  $B$ , and the observed temperature autocorrelation function is

$$C_{obs} = I_{obs} \otimes I_{obs} = (I_{sky} * B) \otimes (I_{sky} * B) = (I_{sky} \otimes I_{sky}) * (B \otimes B) = C_{sky} * C_{beam} = FT(P_{sky} \cdot W)$$

where  $C_{beam}$  is the autocorrelation function of the telescope beam and  $W = FT(C_{beam})$  is called the window function for the telescope.  $*$  and  $\otimes$  indicate convolution and correlation, respectively. For an aperture distribution  $E$ , the beam pattern is

$$B = FT(E) \cdot FT(E) = FT(E * E)$$

and if the beam pattern is symmetric

$$W = FT(B \otimes B) = FT(B * B)$$

$$= FT(FT(E * E) * FT(E * E)) = (E * E)^2$$

CMBR temperature fluctuations can be expanded in spherical harmonics (Peebles 1993; Peacock 1999)

$$\frac{\Delta T(\theta, \phi)}{T_o} = \sum_{l=0}^{\infty} \sum_{m=-l}^l a_{lm} Y_{lm}(\theta, \phi)$$

and assuming rotational symmetry, the expected value of the two-point correlation for fields separated by angle  $\theta$  on

the sky is

$$C_{sky}(\theta) = \frac{1}{4\pi} \sum_{l=0}^{\infty} (2l+1) C_l P_l(\cos \theta)$$

where  $P_l$  are Legendre polynomials and  $C_l = \langle |a_{lm}|^2 \rangle$ .

The observed correlation is

$$C_{obs}(\theta) = \frac{1}{4\pi} \sum_{l=0}^{\infty} (2l+1) C_l P_l(\cos \theta) * C_{beam}$$

$$= \frac{1}{4\pi} \sum_{l=0}^{\infty} (2l+1) C_l W_l P_l(\cos \theta)$$

where  $W_l$  is the azimuthal average of  $W$ . Theoretical predictions and observations are usually quoted as  $\Delta T_l = \sqrt{l(l+1)C_l/2\pi}$  which is a measure of the power per log  $l$ . Fig. 1 shows some measurements of CMBR anisotropy, including the first results from the CBI, along with a  $\Lambda$ -CDM model.

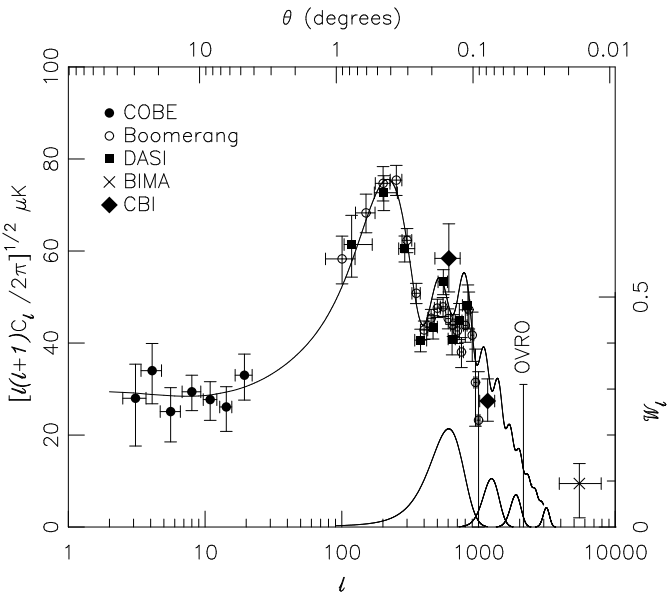


Fig. 1.— Some CMBR anisotropy measurements, shown with a  $\Lambda$ -CDM model with  $\Omega_0 = 1$ ,  $h = 0.70$ ,  $\Omega_b h^2 = 0.02$  and  $\Omega_\Lambda = 0.66$ . At bottom are window functions for 1 m, 2 m, 3 m and 5 m baselines in the CBI. The 1 m baseline is the shortest possible with our 0.9-m diameter antennas and the tracking platform supports baselines up to 5.5 m. The window functions were obtained by computing the azimuthal average of  $(E * E)^2$  using a gaussian approximation to the aperture distribution for a single antenna,  $E_{ant}(r) = \exp(-(2.3r/d)^2)$ . Data points are from COBE (Hinshaw et al. 1996), Boomerang (Netterfield et al. 2001), DASI (Halverson et al. 2001), BIMA (Dawson et al. 2000) and CBI (Padin et al. 2001a). The upper limit (95% confidence) is from OVRO (Readhead et al. 1989). The model was computed using CMBFAST (Seljak and Zaldarriaga 1996, 1997; Zaldarriaga et al. 1998).

For an interferometer with antennas of diameter  $d$  and baseline  $D$ , the window function,  $W_l$ , peaks at  $l \sim 2\pi D/\lambda$  and falls to zero at  $l = 2\pi(D-d)/\lambda$  and  $l = 2\pi(D+d)/\lambda$ . Fig 1 shows  $W_l$  for several CBI baselines.  $W_l = 1$  corresponds to the thermal sensitivity of the interferometer ( $\sim 6 \mu\text{K}$  in 6 hrs for a 1 GHz band in the CBI). The longer baseline interferometers trade sensitivity for better resolution. They instantaneously sample a smaller azimuth range, giving lower peaks in the azimuthally averaged window function,  $W_l$ , and lower sensitivity for measurements

of the power spectrum.

We chose to build an interferometer array for measuring the power spectrum of CMBR fluctuations for several reasons. An interferometer provides a direct measurement of the power in a particular range of multipoles, while in a single dish observation the power spectrum is extracted from measurements of the sky brightness distribution. The approaches are equivalent, but they differ in detail and this provides an important check. Single dish observations which use a switching scheme can reject the total power, and hence 1/f noise from the receiver, only at frequencies below the switching frequency, but an interferometer has the advantage of no total power response on all timescales. An interferometer is a good way of rejecting atmospheric noise, because atmospheric brightness fluctuations tend to wash out as they drift through the fringe pattern (Webster 1994). An interferometer also permits measurements on small angular scales without large optics. The imaging capability of an interferometer is very important for testing, and we used this extensively to help us understand the ground contribution in our observations.

The CBI operates in the 26–36 GHz band, which was chosen as a compromise between receiver sensitivity and contamination from foreground sources. At lower frequencies, point sources and galactic synchrotron and free-free emission are a serious problem, while at higher frequencies, receiver noise temperatures, emission from interstellar dust and atmospheric noise are all increasing. The 325 MHz Westerbork Northern Sky Survey (Rengelink et al. 1997) shows fluctuations in synchrotron emission at  $\sim 2\%$  of the total intensity on scales of a few arcminutes. In the CBI fields, the 325 MHz total intensity is  $\sim 30$  K, so we expect fluctuations in the synchrotron emission to contribute only  $\sim 3 \mu\text{K}$  at 31 GHz. The free-free contribution is limited by  $\text{H}\alpha$  observations (Gaustad et al. 1996) to a few  $\mu\text{K}$ , but the anomalous  $\beta \sim -2$  (where  $\Delta T \propto \nu^\beta$ ) emission from the NCP measured by Leitch et al. (1997) is a potential problem. This anomalous emission is highly correlated with IRAS 100  $\mu\text{m}$  emission (Kogut 1999), so we have chosen CBI fields in regions with 100  $\mu\text{m}$  brightness  $< 1 \text{ MJy sr}^{-1}$ . In these regions, emission from dust is just a few  $\mu\text{K}$  and fluctuations on arcminute scales are substantially less. The diffuse foreground contribution can be extracted using spectral index measurements (Brandt et al. 1994) and for this purpose, the CBI has ten 1-GHz bandwidth correlators covering the 26–36 GHz band. The wide bandwidth also gives high sensitivity. In the case of strong foreground contamination, the sensitivity penalty in extracting the foreground is severe, but our initial CBI observations show no significant contamination.

At high  $l$ , point sources are a serious problem for the CBI. The power spectrum of CMBR fluctuations falls off rapidly with  $l$ , while the point source contribution increases roughly as  $l^2$ . For  $l > 1500$ , CBI measurements are strongly contaminated, so we measure the flux densities of point sources in the CBI fields using a 26–34 GHz Dicke switched radiometer on the 40 m telescope at the Owens Valley Radio Observatory (OVRO). Point source contamination would be significantly lower in the 90 GHz band, and improvements in 90 GHz receivers make this an attractive option for a future upgrade to the CBI.

## 2. THE CBI SITE

The CBI is located at an altitude of 5000 m in the Andes near Cerro Chajnantor, 40 km east of San Pedro de Atacama, Chile. This choice was based largely on our experience with CMBR observations with the OVRO 5 m telescope at 32 GHz and  $l \sim 600$  (Leitch et al. 2000). The sensitivity of the 5 m telescope is limited by atmospheric noise for all but 2 or 3 nights per year, and for the CBI to achieve the thermal noise limit it had to be at a site with about four times less atmospheric noise than OVRO. This implies an altitude of  $\sim 4000$  m, but the estimate is very rough because the noise depends on the distribution of water vapor in the atmosphere (Lay and Halverson 2000). Site testing is the only way to resolve this issue, but a testing phase was not appropriate for a small, short-term project like the CBI, so we had to choose an established site. This narrowed the options to Chajnantor, Mauna Kea and the South Pole. Point source subtraction is a serious problem for the CBI at the South Pole, because there are no high-resolution 30 GHz telescopes available for deep point source surveys in the Southern Hemisphere. Mauna Kea would have involved a long delay and considerable expense, so we chose Chajnantor. Chajnantor is a good millimeter-wave site, has fairly good access and nearby towns provide some infrastructure. However, the environment is aggressive and the combination of high altitude, snow, high winds and low temperatures makes it a difficult place to work. During the period November 1999 to May 2001, we lost about one third of the observing time as storms passed through. (We also had an eruption of Volcan Lascar,  $\sim 40$  km south of the CBI, but fortunately that turned out to be all smoke and no fire!) During the rest of the time, conditions were excellent and the CBI operated at essentially the thermal noise limit.

The Chajnantor site has no infrastructure, so the CBI has its own power plant consisting of a pair of identical 300 kVA diesel generators (Atlas Copco). These are de-rated  $\sim 50\%$  for operation at 5000 m. While one generator is providing power for the telescope, the other is a standby which will start automatically if the first generator fails. We switch generators every week to permit routine maintenance. Fuel consumption is  $\sim 15$  m<sup>3</sup> per month, and we can store up to 40 m<sup>3</sup> on the site. (A large fuel stock is important during the winter, because access for a fuel truck may not be possible for 4–6 weeks following a snow storm.) The buildings at the CBI site are standard ISO shipping containers which are insulated and fitted with heaters and air conditioners, power and lights. The site has a control room, laboratory, 2 bedrooms, bathroom, machine shop and several unfitted storage containers. During routine operations, we usually sleep at the CBI base in San Pedro de Atacama, but stays of 3–4 days at the site are common when the road is blocked with snow. The entire development laboratory for the CBI was shipped with the instrument, so we have good facilities for making repairs and adding new equipment. The oxygen concentration in the control room, laboratory and 2 bedrooms is increased to  $\sim 26\%$  to provide an equivalent altitude of  $\sim 3500$  m (West 1995; Cudaback 1984). Oxygen for the containers is extracted from the outside air using molecular sieves (AirSep Corp.). A 40 ft container requires  $\sim 20$  l min<sup>-1</sup> of oxygen and provides a comfortable working environment for 2 or 3

people. For outside work, we use portable oxygen systems comprising a 415 l oxygen bottle, a 1–4 l min<sup>-1</sup> demand regulator and a nasal cannula (Chad Therapeutics Inc.). These systems are vital to the CBI operation because they enable us to solve complex engineering problems on the telescope.

## 3. ARRAY DESIGN CONSIDERATIONS

The high sensitivity requirements for CMBR observations favor an array with a high filling factor and an attractive option is an instrument which can be equipped with antennas of different sizes. This permits observations on a range of baselines, but always with a fairly close-packed array. In this scheme, the antenna diameter is equal to the shortest baseline, which is in turn set by the smallest  $l$  of interest. The instantaneous resolution in  $l$  corresponds to about half the antenna diameter. Mosaicing (Cornwell et al. 1993) allows the instrument to sample smaller  $l$  and improves the resolution in  $l$ . We use this approach to give a factor 2 or 3 improvement in  $l$ -resolution. The CBI mount was designed to support different array configurations, with baselines up to 5.5 m, and different antenna diameters, so that we could match the sensitivity,  $l$ -range and resolution of the instrument to a particular part of the power spectrum of CMBR fluctuations. The array currently has 0.9-m diameter antennas and a minimum baseline of 1 m, giving an  $l$ -range of  $\sim 600$ –3500 and an  $l$ -resolution of  $\sim 400$  (FWHM), without mosaicing. We have used the antennas in fairly close-packed configurations for maximum sensitivity at low  $l$ , and in a ring-like configuration for fairly uniform sensitivity over the full  $l$ -range of the instrument.

The power spectrum of CMBR fluctuations drops off rapidly for  $l > 300$ , so all baselines in the CBI show a decreasing CMBR signal with increasing frequency. Galactic synchrotron and free-free emission have similar signatures because of their power spectra. Breaking the degeneracy between these effects requires good sampling in  $l$  and is one of the key constraints in choosing a CBI configuration. An alternative approach is to choose baselines that sample the same, or very similar, values of  $l$  at a different frequencies, and we have done this in some CBI configurations.

In a close-packed array, cross-talk between the antennas can be a serious problem. Noise emitted from the input of a receiver can scatter into an adjacent antenna and cause a false signal at the correlator output, as shown in Fig. 2. The false signal limits the sensitivity of the instrument because it is similar to the signals we are trying to measure. In Fig. 2, receiver  $x$  has noise temperature  $T_r$  and emits, from its input, noise power  $pT_r$  which is correlated with the receiver noise. The coupling between the antennas is  $c$  and power  $pcT_r$  is coupled into antenna  $y$ , causing a false signal with maximum amplitude  $T_r\sqrt{pc}$  at the correlator output. Since the coupled noise arrives at the correlator with a delay error, the false signal is reduced by a factor  $\text{sinc}(\pi\tau\Delta\nu)$ , where  $\Delta\nu$  is the bandwidth of the signals at the correlator inputs and  $\tau$  is the delay error (Thompson and D'Addario 1982). The false signal is then  $s = T_r\sqrt{pc} \text{ sinc}(\pi\tau\Delta\nu)$ . This expression is for noise coupling in just one direction, but in practice the process occurs in both directions. If the receivers are identical, the signals for the two directions are complex conjugates,

so the correlator output is always real but the amplitude can be anywhere in the range 0 to  $2s$ , depending on the coupling path length. In the CBI,  $T_r \sim 20$  K,  $\tau \sim 6$  ns and  $\Delta\nu = 1$  GHz so the false signal could be as big as  $2\sqrt{c}$  K. For false signals  $< 1 \mu\text{K}$ , the inter-antenna coupling should be  $< -126$  dB. This is a very stringent requirement and is the key parameter driving the design of the antennas in the CBI.

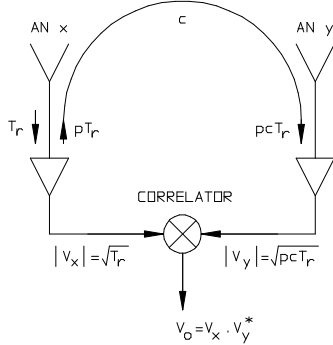


Fig. 2.—Cross-talk between antennas in an array.  $T_r$  is the receiver noise,  $p$  is the correlation coefficient between the outgoing and receiver noises,  $pT_r$  is the outgoing receiver noise which is correlated with  $T_r$  and  $c$  is the coupling between the antennas. (If we transmit  $P_t$  from antenna  $x$  and receive  $P_r$  at antenna  $y$ , then  $c = \frac{P_r}{P_t}$ ). The correlator is a complex multiplier (Thompson et al. 1986).

The cross-talk problem also determined the type of synthesis array we chose for the CBI. In a conventional tracking array, the antennas move with respect to each other, so the cross-talk varies continuously during an observation. This does tend to wash out the cross-talk, but any residual is hard to measure. To avoid this problem, we chose a planar array for the CBI. The antennas are all mounted on a rigid tracking platform so the cross-talk is constant. The platform can be rotated about the optical axis, which allows us to measure cross-talk (and other constant false signals) generated anywhere in the instrument; the false signals rotate with the array, while signals from the sky do not. The additional rotation axis increases the mechanical complexity of the telescope mount, but the signal processing in a planar array is significantly simpler than for a tracking array because there are no fringe rotators or tracking delays. The rotating platform can be used to improve the  $(u, v)$  coverage for an observation and allows us to track a field in parallactic angle, which keeps the response to linearly polarized foregrounds constant. (The receivers in the CBI are configured for circular polarization, but they have  $\sim 10\%$  response to linear polarization at the band edges.) Rotating about the optical axis also permits polarization measurements when some of the antennas in the array are configured for the orthogonal polarization. The instrumental contribution to the response of a cross polarized interferometer rotates with the array, but the contribution from a polarized source is constant if the array tracks the parallactic angle (Conway and Kronberg 1969). Rotating the array relative to the parallactic angle allows the source and instrumental contributions to be separated. The combination of a rotating antenna platform and a configuration with redundant baselines is a powerful tool for identifying false signals, and this feature was used extensively during testing of the CBI.

#### 4. THE TELESCOPE MOUNT

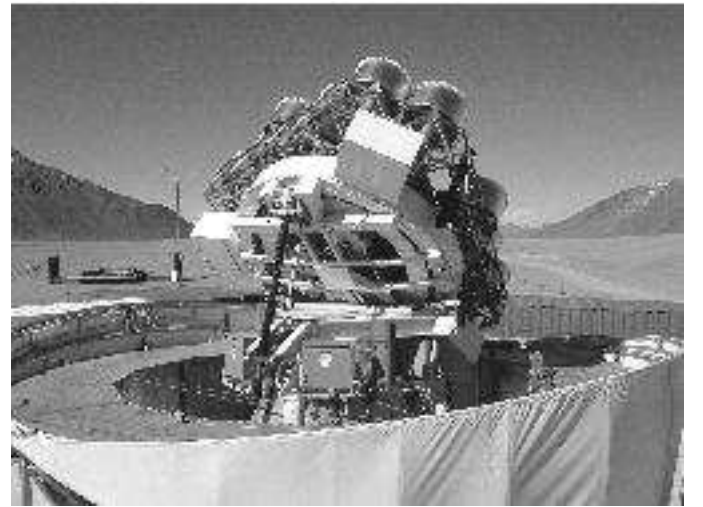


Fig. 3.—Rear view of the CBI. The struts underneath the elevation platform support the parallactic angle cable wrap and the elevation drive motor, which is at the top of the ballscrew. The ballscrew nut is attached to the forks at the back of the azimuth platform. The cables and hoses at the bottom of the elevation platform are part of the elevation cable wrap, which is just behind the elevation axis. The three white boxes attached to the back of the antenna platform contain the signal processing and drive control electronics and uninterruptable power supplies. The 15 cm refractor used for pointing measurements is to the right of the uppermost electronics box.

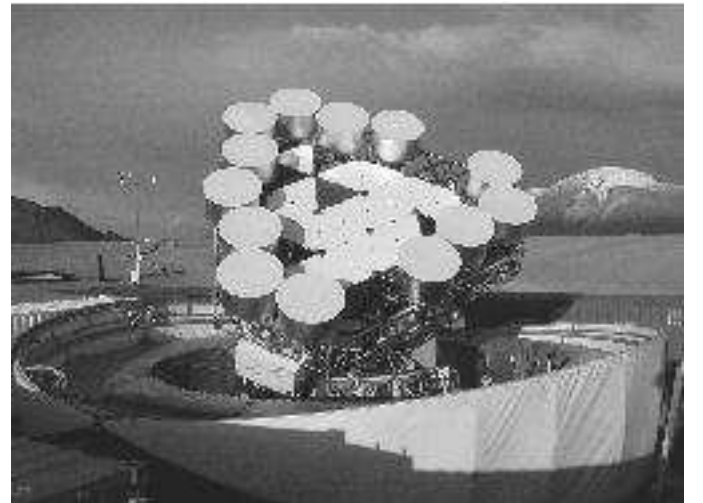


Fig. 4.—Front view of the CBI with the antennas in a ring configuration. This permits easy access to the receivers and was used for testing the CBI and for our first measurements of the power spectrum of CMBR fluctuations. The helium compressors for the refrigerators are at the front of the telescope, on a frame attached to the azimuth platform.

The design of the CBI mount was driven by the conflicting requirements of high pointing accuracy and the need to make a small, fairly lightweight structure that could be transported to a remote observing site. The main effect of pointing errors is to limit the accuracy with which we can subtract point sources from our observations. For any baseline in the instrument, the correlator output, in

temperature units, due to a point source of flux density  $S$  is  $T \sim S\lambda^2/2k\Omega_p$  where  $\Omega_p$  is the primary beam solid angle.  $\Omega_p \sim (\lambda/d)^2$ , so  $T \sim Sd^2/2k$ . A small pointing error  $\zeta$  changes the phase of the correlator output by up to  $\Delta\psi = 2\pi D\zeta/\lambda$  so the maximum residual after subtracting a point source of flux density  $S$  is  $\Delta S = 2\pi SD\zeta/\lambda$ . The residual in temperature units is  $\Delta T \sim \pi Sd^2 D\zeta/k\lambda$ . For a 5.5 m baseline in the CBI,  $\Delta T(\mu\text{K}) \sim 5S(\text{Jy})\zeta(\text{arcsec})$ . The brightest point source in a CBI field is  $\sim 200$  mJy, so for peak temperature residuals of just a few  $\mu\text{K}$ , we require pointing errors of just a few arcseconds. Pointing errors have the biggest effect on the longer baselines where, unfortunately, the microwave background signal is weaker because the power spectrum is falling off rapidly. For measurements on the shorter CBI baselines, the pointing requirements can be relaxed by about an order of magnitude. Mosaicing also requires good pointing, with errors less than a few percent of the primary beamwidth (Cornwell et al. 1993). However, this is not a severe constraint in the CBI because the primary beamwidth is  $\sim 45'$  so pointing errors  $< 1'$  do not seriously limit the dynamic range and fidelity of mosaics.

The conventional approach to achieving arcsecond pointing for a 6 m telescope is a mount that is balanced about all axes. However, this significantly increases the mass and size of the instrument, making transportation to the observing site more difficult. The CBI mount (fabricated by L & F Industries) has no elevation counterweight and weighs only  $\sim 19,000$  kg, which was light enough for us to transport it to Chile without any disassembly. Both the elevation and azimuth axes are unbalanced, but the elevation range is limited to  $40^\circ < el < 89^\circ$  to reduce the effect of deformations. Our observations of the CMBR are made at fairly high elevation to reduce ground pickup and atmospheric effects, so the limited elevation range is not a great disadvantage. The CBI mount is shown in Figs. 3 and 4.

The azimuth axis rotates on a 1.7-m diameter ball bearing which is located at the bottom of the azimuth platform (see Fig. 3). The bearing has a high preload and the change in the center of gravity of the telescope with elevation causes a maximum axial tilt of  $\sim 10''$ . In addition, there is  $\sim 10''$  tilt due to deformation in the base of the teepee which supports the azimuth bearing. We measure and continuously correct the azimuth tilt using a tiltmeter (Applied Geomechanics Inc.) mounted on the azimuth platform in the plane of the azimuth bearing. A 22-bit absolute encoder (BEI), mounted just below the tiltmeter, measures the position of the azimuth axis. The encoder shaft is connected to a post which is attached to the base of the teepee. The azimuth axis is driven by a pair of motors with  $\sim 200$  Nm torque offset. The motor pinions engage a ring gear on the inside of the azimuth bearing and the gear ratio is only 16:1 so the axis is stiff and fast. We use an azimuth slew rate of  $\sim 1$  turn  $\text{min}^{-1}$  and while faster slews are possible, this matches the speed of the other axes. The azimuth (and elevation) drive motors are water-cooled brushless DC motors similar to those used on the Submillimeter Array. They have a peak torque output of  $\sim 1500$  Nm and the motor casing contains a disk brake and a 19-bit encoder which measures the position of the rotor for commutation.

The elevation axis rotates on a pair of 7.5-cm diameter tapered roller bearings. These are standard commercial-grade bearings which we re-housed to provide adjustable preload. The elevation axis is driven by a 7.5-cm diameter ball-screw attached to the elevation platform, with a nut attached to the back of the azimuth platform (see Fig. 3). The ball-screw is clamped directly to the rotor in the elevation motor and since the axis is unbalanced, there is no backlash. To minimize the length of the ball-screw, and hence the height of the mount, we positioned the motor and nut so that the tail of the ball screw moves rapidly away from the teepee as the telescope approaches the zenith. As a result, the elevation gear ratio increases from  $\sim 900$  at  $el = 40^\circ$  to  $\sim 950$  at  $el = 75^\circ$  and then drops rapidly to  $\sim 800$  at the zenith. The disadvantage of this approach is that the elevation servo parameters must be adjusted to compensate for the changing gear ratio. Since the elevation axis is unbalanced, a failure in the drive is potentially catastrophic, so we have two braking systems: an electromechanical disk brake inside the motor casing and a hydraulic brake mounted alongside the ball screw. Both brakes engage in the event of a failure (e.g. open servo loop, power failure, drive speed too high or telescope at a position limit). The hydraulic brake can also be used to lower the elevation platform if the elevation drive motor fails.

In the CBI, the elevation shaft is fixed and the elevation bearing housings, which are attached to the elevation platform, rotate. A 22-bit absolute encoder is attached to one of the bearing housings and the encoder shaft is connected to the end of the elevation shaft. The load on the elevation shaft and bearing housings changes with elevation. This causes the bearing housings to rotate  $\sim 100''$  relative to the elevation platform, and the end of the elevation shaft rotates  $\sim 15''$ . Both rotations affect the elevation encoder reading. In addition to the rotations, there is a  $\sim 25$   $\mu\text{m}$  deflection in the ends of the elevation shaft and this causes a radial misalignment with the encoder axis. The misalignment is taken up by a 15-cm long diaphragm coupling with 3 spring plates. The coupling is folded 3 times so its insertion length is only 5 cm and this permits a very compact, and hence stiff, elevation encoder mount. The rotation of the bearing housings is repeatable, at the level of a few arcseconds, and can be included in the flexure term in the pointing model, but the elevation shaft rotation shows some hysteresis. The elevation bearing housings also rotate  $\sim 30''$  as the antenna platform is rotated. This is due to deformations in the parallactic angle bearing and is repeatable at the level of a few arcseconds. We measure the rotations of the bearing housing and elevation shaft, at the elevation encoder, using linear displacement transducers as shown in Fig. 5, and continuously apply corrections to the requested elevation. This references the outside of the fairly rigid parallactic angle bearing to the azimuth platform. A second tiltmeter, mounted near the transducers which measure the rotation of the elevation shaft, can be used to directly reference the outside of the parallactic angle bearing to the local gravity vector. This corrects deformation in the front of the azimuth platform, which is  $\sim 10''$  over the full elevation range of the CBI. However, the correction cannot be applied continuously because the tiltmeter is  $\sim 2$  m from the azimuth axis and

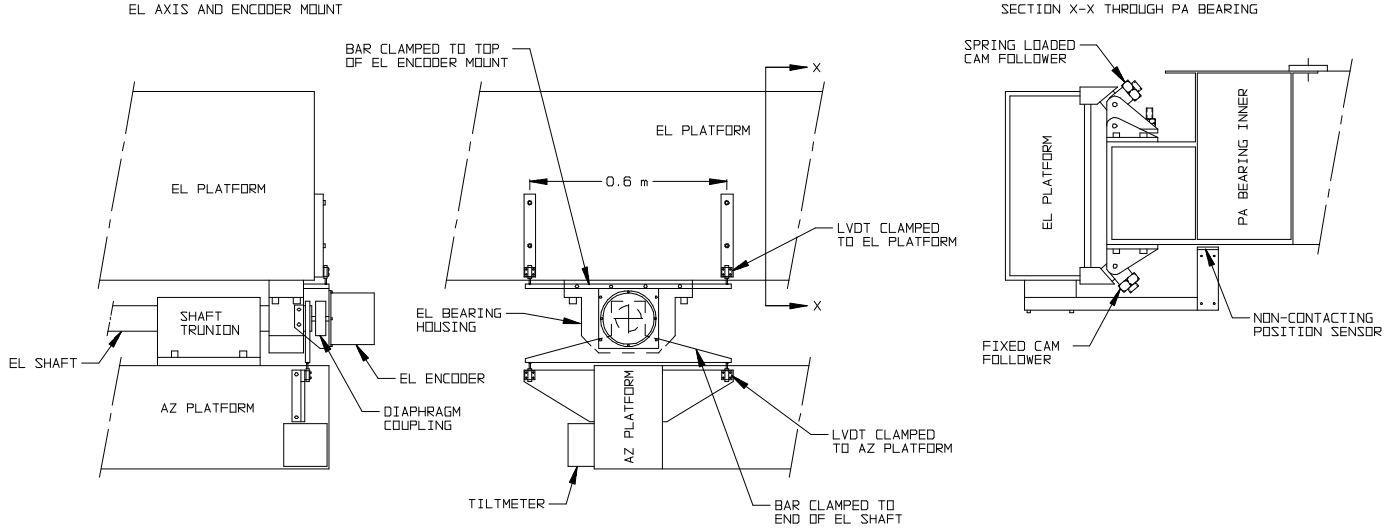


FIG. 5.— Elevation position measurement system. The linear displacement transducers (RDP Electrosense LVDTs) clamped to the azimuth platform measure the rotation of a 0.6-m long bar attached to the end of the elevation shaft. A 1" rotation causes a  $1.5 \mu\text{m}$  change in the position of the LVDT probes. This is a very small displacement, so we make a differential measurement using a pair of probes, which gives high immunity to temperature variations and large-scale distortions in the telescope structure. The probe tips contact small glass plates glued to the ends of the bar to ensure that surface defects do not affect the measurement. The LVDTs clamped to the elevation platform measure the rotation of a bar attached to the encoder mount, which is in turn bolted to the elevation bearing housing. We could significantly reduce the rotation of the end of the elevation shaft (and probably eliminate the rotation measurement) by adding a second trunion on the other side of the bearing housing, but this would be difficult with the current azimuth platform design. The parallactic angle bearing has 4 non-contacting position sensors (RDP Electrosense capacitive sensors) equally spaced round the circumference. We measure the difference between diametrically opposed sensors and compare with measurements made with the telescope at the zenith. We could reduce the elevation dependent tilt of the parallactic angle bearing by increasing the spring force on the top cam followers. However, this increases the torque required to turn the bearing because we use cylindrical cam followers running on conical tracks, so the cam followers must slip as the bearing turns.

the centripetal acceleration during tracking gives unstable tiltmeter readings. To read this tiltmeter, we must stop tracking for a few seconds, but since the tilt varies slowly this only needs to be done every  $\sim 10$  min.

The antenna platform rotates on 40 7.5-cm diameter cam followers which run on a pair of 3.5-m diameter ground tracks (see Fig. 5). The lower track is welded to the elevation platform and is the reference for the parallactic angle axis. The 20 cam followers which run on the lower track can articulate, but their radial positions are fixed. The upper 20 cam followers are spring loaded against the top track and they push the inner part of the bearing against the lower track. At the zenith, the lower track deviates  $\sim 18 \mu\text{m}$  from a circle, so the maximum axial tilt in the bearing is  $\sim 2$ ". There is an additional elevation dependent tilt due to the cam followers sliding radially on the tracks. The effect is mainly in the elevation direction and is  $\sim 3$ " over the full elevation range of the CBI. We measure this tilt using non-contacting position sensors as shown in Fig. 5, but since the effect is small we have not yet included it as a real-time pointing correction. Three steel drive wheels mounted on the elevation platform turn the inner section of the parallactic angle bearing. Each wheel is driven by a stepper motor through a 50:1 worm gearbox with a clutch to synchronize the drives. The required pointing accuracy for the parallactic angle axis is only  $\sim 1'$  so we made no attempt to eliminate backlash in the drive. The position of the parallactic angle axis is measured by a 19-bit absolute encoder (Heidenhain Corp.).

The antenna platform is a hexagonal space frame  $\sim 6$  m in diameter. The frame is 0.75 m thick with 1 m equilateral triangles on the top and bottom surfaces. It is made

from 87 identical rectangular sections which are pinned to rods with a finned node pressed onto each end. Gravitational deformation in the platform, over the full elevation range, with the antennas in a symmetric configuration, is  $\sim 50 \mu\text{m}$  which corresponds to a tilt of  $\sim 2$ ". The entire CBI mount, including the antenna platform, is made of steel so the whole structure has the same expansion coefficient. This is important for operation at the Chajnantor site because the diurnal temperature variation is  $\sim 20$  K and cooling after sunset is rapid, with most of the temperature variation occurring in 1–2 hrs. (Heating after sunrise is slower, typically  $\sim 4$  hrs.)

The pointing model for the CBI is determined from observations of stars using a 15 cm refractor and CCD camera mounted near the edge of the antenna platform. We typically determine the collimation terms for the optical telescope by measuring the pointing errors as a function of antenna platform rotation. Then we measure the pointing errors for  $\sim 25$  stars, uniformly spread over the sky, to determine the encoder offsets, axis tilts (typically  $30$ ") and flexure ( $\sim 30$ " over the full elevation range). A model fit to the pointing measurements typically gives  $\sim 3$ " rms and  $\sim 6$ " peak residuals, with  $\text{az cos(el)}$  and elevation residuals of  $\sim 2$ " rms. Variations in the pointing model during the night, and from night to night, are mainly in the encoder offsets, at the level of a few arcseconds. These variations are partly due to thermal gradients and partly due to non-repeatable changes in the telescope structure. The pointing performance could be improved by using the 15 cm refractor for guiding, but this would restrict observations to clear nights. In addition to the 15 cm refractor, we have two 5 cm refractors with CCD cameras, one

mounted at the center of the antenna platform and one on the elevation platform, just above the elevation encoder. Pointing measurements with all 3 optical telescopes allow us to measure deformations in the antenna platform and parallactic angle bearing, which are at the level of a few arcseconds. Short-term tracking errors are typically  $\sim 3''$  peak in azimuth and elevation. The dominant error has a period of one motor commutation cycle and is due to gain and offset errors in the drive amplifiers and torque ripple in the motors. Since the azimuth drive motors have a high torque offset and the elevation platform is unbalanced, the azimuth and elevation axes are very stiff and we do not see any degradation in tracking with wind gusts up to  $\sim 15$  m s $^{-1}$ .

The CBI drives are controlled by a PMAC computer (Delta Tau Data Systems Inc.). This is designed for controlling multi-axis machine tools, but it provides many of the functions required for telescope control. The PMAC receives requested positions from the CBI real-time control system every second. It moves the axes as requested, commutating the motors, checking position, velocity and acceleration limits and monitoring the status of amplifiers, motors and encoders. It also sets the servo loop parameters, which are different for slewing and tracking and, in the case of the elevation axis, vary with axis position. The speed of the axes is controlled by a crystal oscillator and a trigger pulse from a GPS clock is used to synchronize the PMAC each time a new source is observed.

The azimuth range of the CBI is  $-180^\circ < az < 270^\circ$ , which was chosen to avoid long slews between the target source and calibrators for most observations. The parallactic angle axis also has a range of  $1\frac{1}{4}$  turns, but some long slews are unavoidable because in addition to tracking in parallactic angle, we also rotate the antenna platform to improve the  $(u, v)$  coverage. The azimuth cable wrap is inside the teepee and is of the coiled-spring design. This wrap carries power, cooling water for helium compressors and electronics and optical fibers for communications with the telescope control computer. The parallactic angle cable wrap is more complicated because it has to fit inside the bearing structure while carrying 26 helium lines for the receivers, power, cooling water and many drive control cables. The wrap overlays 42 cables in 3 layers on a central drum, with the cables supported on 3 satellite drums, kept in tension by coiled springs. A key advantage of this design is that the cables in the moving part of the wrap are only  $\sim 3$  m long (compared with  $\sim 15$  m for the coiled-spring azimuth wrap). This helps to minimize the pressure drop in the helium lines in the wrap.

The CBI is housed in a retractable dome (manufactured by American Space Frames Inc.) which protects the instrument and workers from the weather. The dome is a 12-m diameter hemispherical steel space frame covered with polyethylene cloth (see Fig. 6). It has 8 segments which nest inside each other, 4 on each side, when the dome is open (see Figs. 3 and 4). To close the dome, the top 4 segments are raised on cradles and then wire ropes pull the top 2 dome segments together and up. As a segment rises, tangs on the bottom engage the top of the next segment in. A pneumatic clamp at the top of the dome holds the 2 halves of the hemisphere together and the bottom segments are clamped to the top of the walkway that sur-

rounds the telescope. The walkway provides easy access to the electronics boxes on the antenna platform. The dome is a fairly light, flexible structure and the  $\sim 5$  cm gaps between segments prevent large pressure differences building up, even in very high winds. The structure has withstood storms lasting 3 days with wind speeds up to 45 m s $^{-1}$ . Under these conditions, the cloth segments tend to pull away from the steel frame. This reduces the cross-section of the segments and limits the wind loading, preventing serious damage to the steel structure. Usually, we do not observe if the wind speed is much above  $\sim 15$  m s $^{-1}$  because it is difficult to open and close the dome in strong gusty wind.

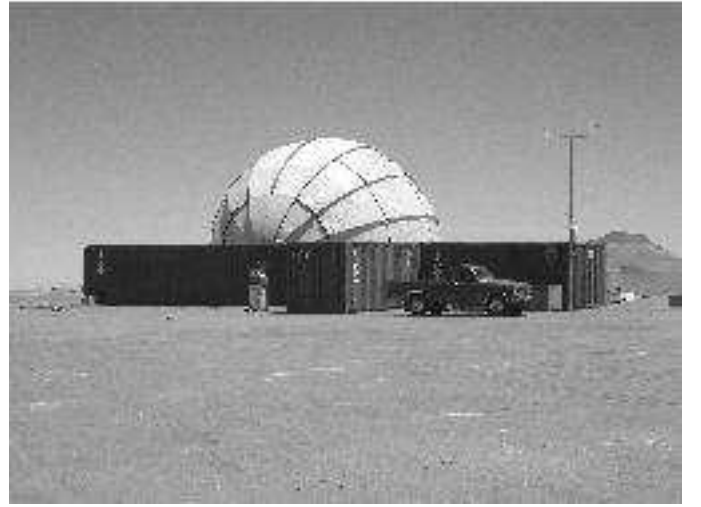


Fig. 6.—The CBI site with the dome closed.

## 5. ANTENNAS

The main constraint on the design of the CBI antennas is low cross-talk. This requires antennas with very little scattering, suggesting an unblocked design. Corrugated feedhorns have ideal performance characteristics, but are somewhat impractical for a  $\sim 1$  m aperture. A lens would be required to reduce the horn length and loss in the lens would seriously degrade the sensitivity of the instrument. Offset reflectors are also an obvious choice, but they are difficult to close-pack and access to the receivers is awkward. Because of these problems, we used the shielded cassegrain design shown in Fig. 7. This has a 0.9-m diameter  $f/0.33$  machined cast aluminum primary, and all 13 primaries made for the CBI have very small surface profile errors. Based on 6298 measurements, evenly spaced across the surface of each primary, using a Zeiss Coordinate Measuring Machine, the deviation from a paraboloid of focal length 0.3002 m ranges from 110  $\mu\text{m}$  rms ( $\lambda/88$  at 31 GHz) for the first 3 primaries made, down to 30–40  $\mu\text{m}$  rms ( $\lambda/322$ – $\lambda/242$  at 31 GHz) for the last 10 primaries. The 0.155-m diameter secondary is made of carbon fiber epoxy and weighs only  $\sim 80$  g. It is supported on four feedlegs made of expanded polystyrene. The feedlegs have a U cross-section, hot-wire cut from 2 lb ft $^{-3}$  expanded polystyrene stock. During assembly of the antenna, the secondary is supported on a fixture attached to the primary, and the secondary and feedlegs are glued in place. The polystyrene feedlegs cause very little scatter-

ing and contribute only  $\sim 0.5$  K to the system noise. The cassegrain antenna sits in the bottom of a deep cylindrical shield which reduces cross-talk due to scattering from the secondary and the cryostat. Scattering from the rim of the shield is reduced by rolling the rim with a radius of  $\sim 5\lambda$  (Mather 1981). The shield is made from a sheet of  $1/16$ " aluminum, welded into a cylinder and then spun to form the rolled rim. The height of the shield was chosen so that the rim intercepts the beam where the electric field is about one tenth of the on-axis field. This reduces the forward gain of the antenna by  $\sim 1\%$ . Ohmic losses in the shield, measured using room temperature and liquid nitrogen loads in front of antennas with shields of different heights, contribute  $\sim 0.5$  K to the system noise. A 0.36-mm thick woven teflon window (W.L. Gore Inc.), attached to the front of the shield, protects the antenna components from the weather. This window contributes  $\sim 0.5$  K to the system noise, so the total antenna contribution is  $\sim 1.5$  K. The antenna is fed by a wideband corrugated horn at the cassegrain focus, illuminating the secondary with a  $-11$  dB edge taper. The horn has a semi-flare angle of  $15^\circ$  and an aperture of  $8.4\lambda$  at the band center. The  $-3$  dB beamwidth of the horn varies by only  $\sim 1\%$  over the 26-36 GHz band, so the efficiency of the antenna is essentially independent of frequency. A  $15^\circ$  semi-flare angle minimizes the horn aperture for approximately constant beamwidth over the band (Clarricoats and Olver 1984). This in turn minimizes the diameter of the secondary, but the blockage is still quite high at  $\sim 2\%$  and this degrades the efficiency of the antenna by  $\sim 4\%$  (Kildal 1983).

The measured half-power beamwidth of a CBI antenna varies from  $51'$  at 26 GHz to  $38'$  at 36 GHz and the first sidelobe is  $\sim -18$  dB. Offsets between the antenna boresights are a few arcminutes and are determined primarily by machining tolerances in the feedhorn mounts. The antenna beams can be aligned by adjusting the receiver mounts, but usually we just measure the beam for each baseline and band. The cross-talk between a pair of touching antennas has a peak value of  $-100$  dB at the low frequency end of the band, decreasing to  $-115$  dB at the high frequency end (Padin et al. 2000). This is  $\sim 30$  dB better than for antennas without shields. In any 1 GHz CBI band, the average cross-talk is at most  $-110$  dB, so the maximum false signal is  $6 \mu\text{K}$  with 20 K receivers. The actual false signal will be smaller, because the noise emitted from a receiver input is not completely correlated with the receiver noise. Unfortunately, a direct measurement of the false signal is difficult, because ground pickup dominates the correlator output for the short baselines in the CBI. Between the feedhorn and receiver, there is a rotating half-wave plate phase shifter which is included to provide additional rejection of the cross-talk between antennas (and is also useful for identifying unwanted signals which do not enter through the feedhorn). If all the phase shifters in the array are rotated synchronously, the correlator output due to signals from the sky does not change, but the phase of the contribution due to cross-talk changes by twice the phase change introduced by each phase shifter. At the band center, the phase shifters have a range of  $\pm 2\pi$  and rotating all the phase shifters through  $N$  turns in an integration period completely rejects the cross-talk. At the band edges, a single turn per integration reduces

the correlator output due to cross-talk by about a factor 10. Any stable residual false signals can be measured by rotating the entire array about the optical axis.

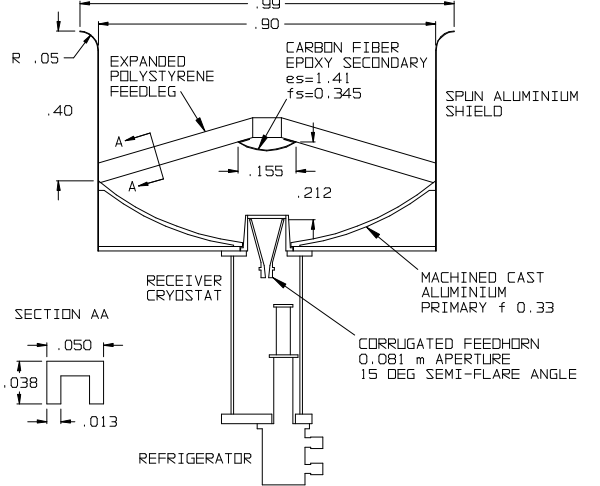


Fig. 7.—Cross-section of a CBI antenna. Dimensions are in meters.  $es$  and  $fs$  are the eccentricity and focal length of the secondary. The top of the cryostat is bolted to the back of the antenna and three tensioned struts run from the bottom of the cryostat to the antenna platform to stiffen the assembly.

Most of the possible CBI array configurations have many  $\sim 1$  m baselines. These are most sensitive to emission on  $\sim 30'$  angular scales, so the Sun and Moon cause serious problems for the CBI. The Sun is so bright that it completely dominates the CMBR signal, and the CBI is restricted to night-time observations. The Moon can be a problem if it is  $<60^\circ$  from the optical axis of the telescope. At  $60^\circ$ , the primary beam response is  $\sim -70$  dB and the Moon gives a  $\sim 10 \mu\text{K}$  signal on a 1 m baseline. Emission from the ground is also a problem and is particularly serious if the fringe pattern for a short baseline stays roughly parallel to the horizon as the array tracks the target field. In this case, the ground signal at the correlator output can be  $\sim 1$  mK and may be roughly constant for tens of minutes. The ground signal is very repeatable, even on timescales of several hours, so we can measure the difference between two adjacent fields to remove the ground contribution. Typically, we observe the target field for 8 min and then switch to a trailing field at the same declination, but 8 min later in right ascension. The two fields are observed over exactly the same azimuth-elevation track, so they have identical ground contributions. This approach gives difference maps and reduces the sensitivity of the instrument by  $\sqrt{2}$  for CMBR observations and 2 for other observations. (The sensitivity degradation is less for CMBR observations because both the target field and trail field have CMBR fluctuations and the rms of the difference between the fields is  $\sqrt{2}$  larger than the rms for either field.) For observations of the Sunyaev-Zel'dovich effect, CMBR fluctuations in the trail field are a serious contaminant, so we also observe a lead field and take the difference between the target field and the average of the lead and trail fields. This reduces the sensitivity by a factor  $3/\sqrt{2}$ . Ground signals also degrade the system noise temperature. At the zenith, the spillover contribution is

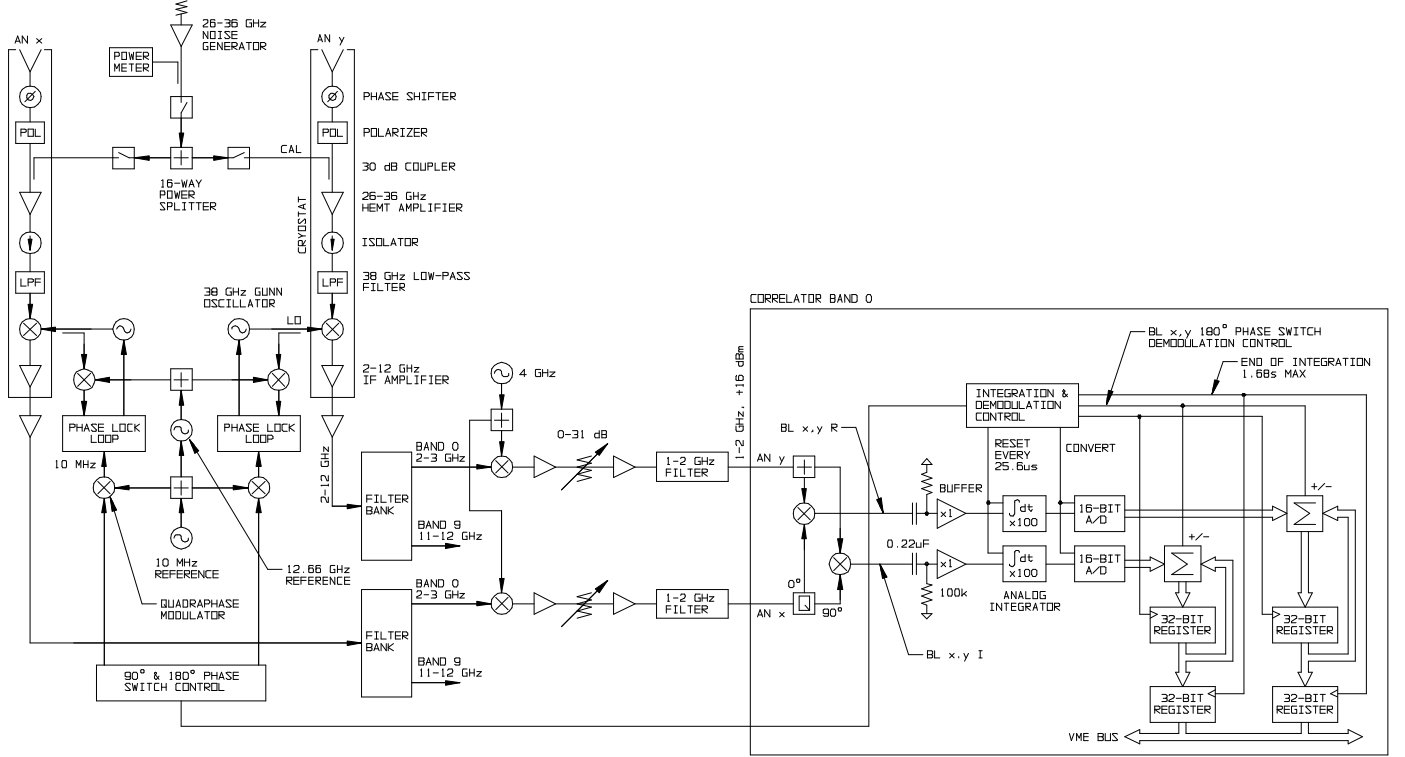


FIG. 8.— Signal processing in the CBI. Receiver details are shown for 2 antennas, x and y, and for band 0 of the downconverter. Correlator readout details are given for just one baseline (x, y) in band 0. + is a power splitter and Q is a quadrature hybrid.

only  $\sim 1$  K, but this increases to  $\sim 5$  K at  $40^\circ$  elevation, because ground emission reflects off the inside of the antenna shield cans and enters the receiver feedhorns. We could improve the sensitivity of the CBI by building a ground shield, but the required structure is  $\sim 10$  m high and  $\sim 25$  m in diameter. The cost of a rigid structure of this size is prohibitive and the high winds and heavy snowfalls we experienced during our first year of operation make a flexible shield impractical.

## 6. SIGNAL PROCESSING

Each antenna in the CBI has a cooled heterodyne receiver with a 26-36 GHz InP HEMT amplifier, Schottky mixer and a 2-12 GHz IF amplifier. The receiver details are shown in Fig. 8. All the receiver components, including the feedhorn, are cooled to  $\sim 8$  K using a 2-stage Gifford-McMahon refrigerator (APD Cryogenics Inc.). The 1st stage of the refrigerator is at  $\sim 40$  K and cools the cryostat radiation shields and heatsinks for the receiver wiring. Compressed helium for the refrigerators is supplied by 7 scroll compressors located on the telescope azimuth platform, with each compressor driving 2 refrigerators. The 26 helium lines (for 13 receivers) run through both the elevation and parallactic angle cable wraps.

Between the rotating half-wave plate phase shifter at the feedhorn output and the HEMT amplifier input, there is a quarter-wave plate circular polarizer with a mode suppressor. The half and quarter-wave plates are tapered teflon slabs glued into 8-mm diameter circular waveguide (Ayers 1957). Deviations from quarter-wave are  $\sim 5^\circ$  at the band edges, which corresponds to a polarization leakage factor of  $\sim 0.1$ . The mode suppressor is a tapered piece

of mica resistance card, glued into small broached slots in the circular waveguide, with the card parallel to the unwanted electric field. This attenuates the unwanted polarization by  $\sim 40$  dB, reducing reflections between the input of the HEMT amplifier and the antenna which increase the response of the receiver to the unwanted polarization. The rotating half-wave plate runs in ball bearings and has chokes at the interface between the rotating and fixed sections of waveguide. The rotating section is positioned by a stepper motor and encoder, which are inside the cryostat but at room temperature. The insertion loss of the complete half and quarter-wave plate and mode suppressor assembly is  $\sim 0.15$  dB at 8 K.

Cooling the feedhorn imposes tight constraints on the design of the cryostat window because the feedhorn mouth is in front of the primary and the size of the cryostat surrounding the feedhorn sets the minimum blockage for the antenna. The cryostat window must be thin, so that the cryostat wall is as far away as possible from the secondary, but the window must be strong enough to support atmospheric pressure and must attenuate infra-red radiation enough to prevent excessive heat loading. These constraints are difficult because the window is  $\sim 10$  cm in diameter. We use a 0.05-mm thick mylar film stretched and glued between two thin stainless-steel rings (like a drum skin) to support a  $2\text{lb ft}^{-3}$  expanded polystyrene infra-red block. The infra-red block is 1 cm thick at the edge and the inside face is tapered to increase the thickness to 2 cm at the center, to prevent the polystyrene from cracking under load. The vacuum window is 3-mm thick closed-cell expanded polyethylene foam. This rests on the flat outside face of the infra-red block and is clamped directly to

the cryostat wall without an o-ring seal. The wall of the cryostat and the vacuum window retaining ring are very close to the feedhorn mouth, and to reduce scattering, the inside surfaces are grooved to form a corrugated circular waveguide extending  $\sim 1.5$  cm in front of the feedhorn.

The sensitivity of the CBI is set primarily by the noise temperature of the 26–36 GHz HEMT amplifiers. These are 4-stage amplifiers with  $100\ \mu\text{m}$  InP HEMTs, giving  $\sim 30$  dB gain and amplifier noise temperatures in the range 13 K, at the center of the band for the best amplifier, to 25 K, at the edge of the band for the worst amplifier (Pospieszalski et al. 1994, 1995). The cooled downconverter contribution to the receiver noise varies from  $\sim 2$  K at 26 GHz to  $\sim 0.5$  K at 36 GHz. Loss in the phase-shifter and polarizer add  $\sim 1$  K, the antenna contribution is  $\sim 1.5$  K and ground spillover at the zenith  $\sim 1$  K. Under good observing conditions, the atmosphere at the Chajnantor site contributes  $\sim 1$  K, so with 2.7 K from the CMBR, the system noise temperature is in the range 21–34 K.

Signals from the 13 antennas in the CBI are cross-correlated in an analog correlator with a filterbank architecture (Padin et al. 2001b). The analog filterbank approach was chosen to keep the cost and size of the system down and to give high correlator efficiency, but it does require a calibration scheme to measure gain and phase errors in the multipliers. The 2–12 GHz signals from the cooled downconverter in each receiver are split into ten 1 GHz bands by a bank of filters. Each 1 GHz band is then downconverted to 1–2 GHz, which is the operating band for the multipliers. The details of the downconversion scheme are shown in Fig. 8.

Each baseline in the array requires a complex multiplier to measure the cross-correlation for each band. This involves distributing many 1–2 GHz signals between antennas and multipliers, and finding an efficient architecture was one of the key design challenges in the CBI. The CBI correlator uses the square array of multipliers shown in Fig. 9 to measure all the cross-correlations for a band. In this scheme, the top right half of the array measures the real parts of the cross-correlations, and the bottom left half measures the imaginary parts. The array has just one quadrature hybrid per antenna, so the circuit is very compact. Signals from the antennas are distributed by a grid of microstrip transmission lines, with a 4-GHz bandwidth Gilbert Cell multiplier (Gilbert 1974) at each crossing point. The signals are sampled by  $800\ \Omega$  tap resistors, which form potential divider circuits with the  $50\ \Omega$  input impedance of the multiplier chips. The multipliers are linear for input powers below  $\sim -15$  dBm, but at  $\sim -20$  dBm, noise from the post-multiplier amplifiers degrades the efficiency of the correlator by  $\sim 2\%$ . Thus, we can tolerate a power variation of only  $\sim 3$  dB over the multiplier array, which requires tap resistors  $\geq 800\ \Omega$ . A larger tap resistance would give smaller power variations over the array, but at the expense of higher input power. With  $800\ \Omega$  tap resistors, the input power is  $+16$  dBm, which is easy to provide. The multiplier array is made entirely of chip components, glued to a  $97 \times 69$  mm substrate, with  $25\text{-}\mu\text{m}$  diameter wirebond connections. The grid spacing is 5 mm; set primarily by the size of the coupling capacitors at the multiplier inputs and the pins which take the multiplier output signals through the bottom of

the multiplier box. This puts the first Bragg reflection at  $\sim 10$  GHz, which is well above the operating band of the multipliers. The 5 mm grid spacing leaves very little space for the quadrature hybrids and power splitters in the signal distribution, so these are realized using lumped elements. The power splitters have a 3-pole low-pass filter in each arm and the quadrature hybrids comprise a power splitter followed by  $+45^\circ$  and  $-45^\circ$  phase-shift networks. Sensitivity degradation due to passband errors in the correlator signal distribution is just a few percent. (A 3 dB p-p passband error causes a 5% degradation in sensitivity (Thompson and D'Addario 1982) and typical passband errors in the power splitters and hybrids are  $\sim 0.2$  dB p-p and  $\sim 1$  dB p-p, respectively.) The array of multipliers also includes tunnel-diode total power detectors for each antenna. These are used to set the correlator input power, to ensure the correct operating point for the multipliers, and for receiver noise temperature measurements using hot and cold loads.

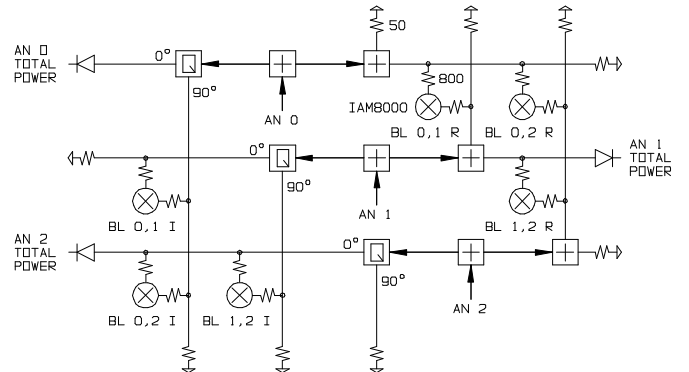


Fig. 9.—Architecture of the CBI correlator. This diagram shows a multiplier array for just 3 antennas. The CBI correlator uses a similar, but larger, array with 13 antenna inputs and 156 multipliers. The antenna inputs are along the diagonal, and for a square array, the path lengths to the 2 inputs of a multiplier are the same.

For observations of CMBR anisotropies, we cannot tolerate false signals bigger than a few  $\mu\text{K}$ , so with  $\sim 25$  K system noise temperatures, the effective cross-talk between the multiplier inputs in the correlator must be  $< -140$  dB. This limit applies to all sources of cross-talk e.g. in the receiver and downconverter local oscillators, IF amplifiers and in the correlator itself. In most parts of the instrument, low cross-talk can be achieved easily, but the performance of the correlator is limited by cross-talk in and between the multipliers, which can be as much as  $\sim -40$  dB. False signals due to cross-talk in the signal processing electronics, and mains pick-up at the multiplier outputs, are rejected using a  $180^\circ$  phase-switching scheme in which the receiver local oscillators are inverted in Walsh function cycles (Urry et al. 1985). This modulates the sign of the multiplier outputs for the desired signals and demodulation rejects the false signals. In the CBI, the Walsh functions have a maximum sequency of 32 and a period of  $25.6\ \mu\text{s}$  (i.e. 0.82 ms for a complete 32-state cycle), so even quite rapidly varying false signals are strongly rejected. Each multiplier output has a high-pass RC filter which removes the multiplier DC offset and any DC components generated by cross-talk. This is followed by a  $25.6\ \mu\text{s}$  analog box-car integrator and a 16-bit analog-to-digital

converter. The subsequent signal processing, which includes the Walsh function phase-switch demodulation and integration for up to 1.68 s, is entirely digital and is handled by an array of field-programmable gate arrays. The CBI correlator, including power supplies and water to air heat exchangers for cooling, occupies about half of a 12U VME crate.

The efficiency of the CBI correlator, measured using 1–2 GHz noise sources to simulate the receivers and the signal, is in the range 0.9–1. The efficiency of the entire receiving system, measured with room temperature loads at the receiver inputs and the noise calibration source in Fig. 8 as a correlated signal, is in the range 0.8–1, depending on the passband errors for the channel. A typical image made with the instrument has a noise level within  $\sim 20\%$  of the thermal noise. False signals due to cross-talk in the instrument are at the level of just a few  $\mu\text{K}$ . In a 3-receiver test, with room-temperature loads at the receiver inputs, the average of the 3 real and imaginary channels was  $0.6 \times 10^{-7}$ , in units of correlation coefficient, after integrating for 20 hrs. The largest correlator output, in a real or imaginary channel, was  $2.2 \times 10^{-7}$ . This is  $\sim 3$  times the rms, so it is still consistent with a mean correlator output of zero, but if it were a residual false signal, the level would be just  $6 \mu\text{K}$  with 25 K system noise temperatures. The residual false signal can be removed by rotating the antenna platform during an observation, or by measuring the difference between 2 fields (see Sec. 8). Quadrature errors in the correlator are typically  $\sim 1$  dB and  $\sim 5^\circ$ , with a worst-case of 3 dB and  $15^\circ$ . The quadrature errors must be measured in order to calculate the actual cross-correlation from the correlator outputs (Padin et al. 2001b). This is done by injecting a correlated signal from the noise calibration source in Fig. 8 and sequentially changing the phase of each receiver local oscillator by  $90^\circ$ . The receivers have phase-locked Gunn local oscillators with a quadrature modulator in the reference for the phase-lock loop. The modulators are used for correlator quadrature error measurements and for the  $180^\circ$  Walsh function phase-switching scheme. A quadrature error measurement takes  $\sim 4$  min and we typically do this twice per day. Variations in the quadrature errors are  $\sim 2\%$  and  $1^\circ$  p-p on timescales of a day to a month.

All the signal processing electronics are mounted on the antenna platform to eliminate instability due to moving cables. The electronics boxes are also temperature controlled to  $\sim \pm 1$  K using water to air heat exchangers. Gain and phase variations in the instrument are measured every  $\sim 10$  min using the noise calibration source, which is in turn calibrated using daily observations of planets, quasars, radio galaxies and supernova remnants. The calibration noise is injected as early as possible in the receiving system so that only the feedhorns, phase-shifters and polarizers are outside the measurement loop. A diode power sensor measures variations in the output of the noise calibration source and the noise distribution components have low temperature coefficients and are temperature controlled to  $\sim \pm 3$  K. (The noise distribution and local oscillator reference cables run in plastic conduits along with a cooling water hose.) Variations in the calibration of the CBI, due to variations in the noise distribution components, are at the 1% and  $1^\circ$  level. Since the injection point for the

calibration noise is ahead of the receiver local oscillators, phase-switching offers no rejection of cross-talk between the receivers through the noise calibration source. The diode switches at the outputs of the 16-way power splitter in Fig. 8 are included to give high isolation between the receivers when the noise is off, but these switches limit the stability of the calibration scheme.

## 7. CONTROL AND MONITORING

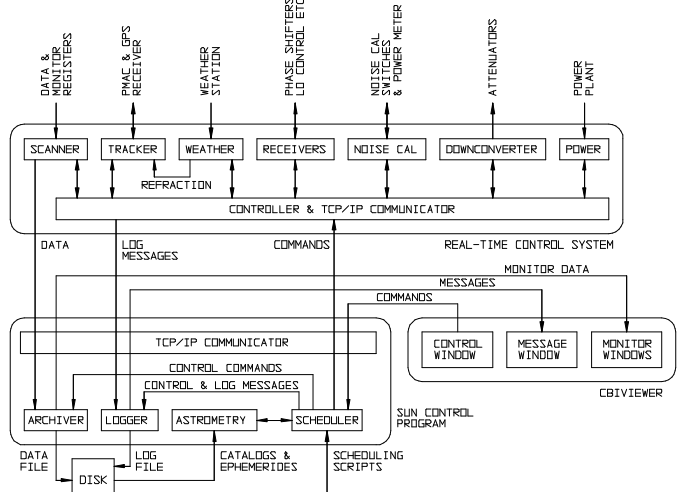


Fig. 10.—The CBI control system.

Fig. 10 shows a block diagram of the CBI control system. Telescope control, data collection and monitoring functions are handled by a real-time control system running under VxWorks (Wind River Systems Inc.) on a Motorola 68060 computer. The scanner task reads all 1690 correlator channels (156 multipliers plus 13 total powers for 10 bands) and about the same number of monitor points (e.g. receiver temperatures and telescope position) typically every 0.84 s. The tracker calculates the required telescope position every second and the other tasks control the instrument set-up (e.g. the positions of the phase shifters in the receivers and the settings of the attenuators in the downconverter). A control program running on a dedicated Sun workstation schedules operation of the real-time control system, manages source catalogs and ephemerides, archives data and handles communications with “cbiviewer” user interface programs. Cbiviewer includes a terminal window for entering control commands and submitting observing schedules and provides a powerful graphical interface for monitoring data and the state of the CBI. Multiple cbiviewer connections are allowed so the instrument can be controlled and monitored from different locations simultaneously. For most observations, we integrate the data for 8.4 s before archiving, but for fast operations, such as noise calibrations and optical pointing measurements, we archive 0.84 s integrations. The data rate is typically 100 MB/day and we archive on 4 GB magneto-optical disks. The magneto-optical disks are used to transport data from the CBI site. We also have a modem connection via a cellphone, which permits remote monitoring of the weather station, power plant and cryogenics. The CBI can operate unattended, except for opening and closing the dome, and cbiviewer has a pro-

grammable alarm which summons the observer if the telescope stops tracking or if a monitor (e.g. wind speed) is out of range.

## 8. OBSERVATIONS

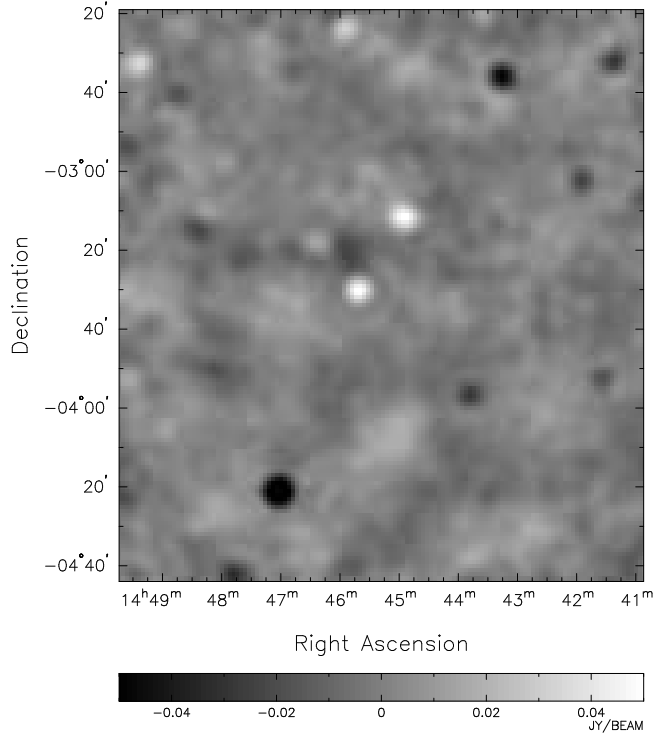


Fig. 11.—Mosaic of the 14<sup>h</sup> CBI field made from 42 main-trail observations ( $\sim 200$  hrs total observing time). All 10 frequency bands have been combined and the individual maps for each pointing center have been corrected for their primary beams. The mosaic was made pixel-by-pixel by summing the individual maps, weighting by the inverse variance. The rms noise in the mosaic varies from 1.5 mJy/beam in the central area to  $\sim 5$  mJy/beam at the edges. The synthesized beamwidth varies from 4.7' to 5.3' (FWHM). The brightest point source in this image has a flux density of  $-96$  mJy.

Our current CMBR observations are in three  $2^\circ \times 2^\circ$  fields separated by  $\sim 6$  h in right ascension. The fields were chosen to have IRAS 100  $\mu$ m emission  $< 1$  MJy sr $^{-1}$ , low synchrotron emission and no point sources brighter than a few hundred mJy at 1.4 GHz. Each night, we observe the two fields that are visible, along with several amplitude and phase calibrators. Virgo A, Taurus A and Jupiter are our primary amplitude calibrators. To permit subtraction of the ground contribution (and any constant false signals generated in the instrument) observations are broken up into scans with 8 min on the main field, and 8 min on a trailing field at the same declination, but 8 min later in right ascension. The main and trail fields are observed over the same azimuth-elevation track and the difference between the two fields shows no evidence of ground contamination. For example, dividing the observation into rising and setting halves yields similar images (with similar noise outside the primary beam) for the differenced fields, even though the main and trail field images show quite different ground contributions for the two halves of the observation (Padin et al. 2001a). The noise calibra-

tion source is fired for 10 s at the beginning and end of each 8 min scan and just before each calibration observation. Gain and phase variations during a 6 h observation are at most 10% and 5° p-p before the noise calibration is applied, and typically 1% and 1° p-p after calibration. During an observation, the array continuously tracks the parallactic angle and is rotated 20° or 30° after each main and trail scan pair. This improves the synthesized beam and permits polarization measurements. We build a mosaic on a grid of pointing centers spaced 20' and observe for one night on each grid point. Fig. 11 shows a mosaic of the 14<sup>h</sup> CBI field made from 42 pointings. The extended structures in this image are fluctuations in the CMBR. They are most obvious on scales of a few tens of arcminutes because the CBI has low sensitivity to larger angular scales and the power spectrum of CMBR fluctuations falls off rapidly on smaller angular scales. Since the image is a difference between main and trail fields, point sources can appear either positive or negative.

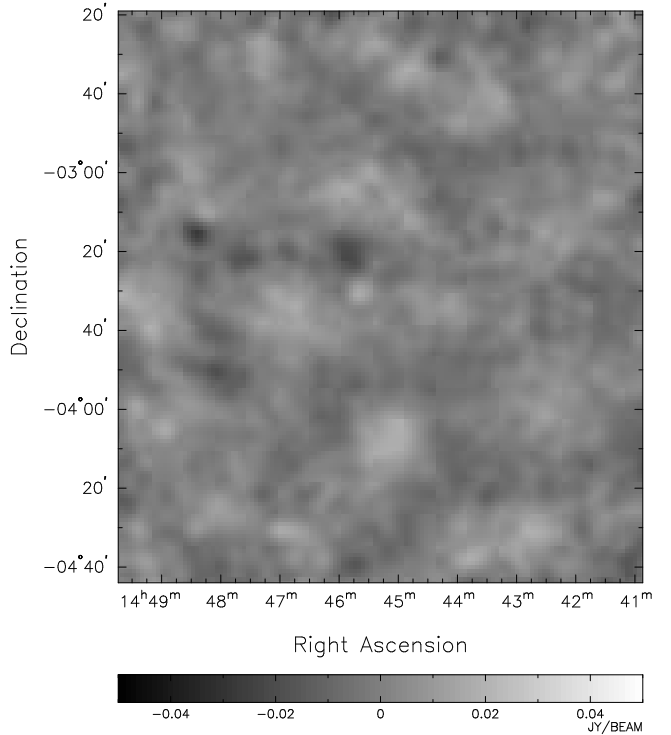


Fig. 12.—The 14<sup>h</sup> field after removal of 63 point sources monitored by the OVRO 40 m telescope.

An accurate measurement of the primary beam is required for the power spectrum extraction, and for making mosaiced images. Errors in the beam area affect the scaling of the power spectrum, while errors in the beam shape, and hence errors in the window function, can distort the power spectrum. We measure the primary beam using observations of Taurus A on a grid of pointing centers spaced 7'. With an integration time of 30 s per pointing, the signal-to-noise ratio on boresight is  $\sim 300$ , so the error on a measured point on the beam profile is  $\sim 0.01$ . The integration time can be increased with distance from the beam center to improve the signal-to-noise ratio in the outer part of the beam. The measured beamwidth varies from 51' to 38' (FWHM) across the 26–36 GHz band, and

in any 1 GHz band, the standard deviation of the FWHM beamwidths for the 78 baselines in the array is  $\sim 0.3'$ . For a particular baseline, the offset of the beam center is typically a few arcminutes and varies by  $\sim 1'$  across the 26–36 GHz band. Some of these variations with baseline and frequency are real changes in the beams, so  $0.3'$  and  $1'$  are upper limits to the errors on the beamwidth and offset.

Flux density measurements of point sources in the CBI fields brighter than  $\sim 6$  mJy at 31 GHz are made using the OVRO 40 m telescope. These measurements are made within a few days of the CBI observations because many of the sources are variable. We monitor sources in the NRAO VLA Sky Survey (Condon et al. 1998) with flux densities  $\geq 6$  mJy at 1.4 GHz. The very weak and inverted-spectrum sources that we miss do not seriously contaminate CMBR power spectrum measurements for  $l < 1500$ . At higher  $l$ , we must make a statistical correction for the unmeasured sources based on number counts from deep VLA observations of the  $8^h$  CBI field. For  $l < 2000$ , we can use the longer baselines in the CBI to monitor point sources. The advantage of this approach is that the CMBR and point source observations are simultaneous and have the same pointing and flux scale errors. Fig. 12 shows the  $14^h$  field after removal of the point sources monitored by the OVRO 40 m telescope. Residual point source contamination in this image is small, indicating that the flux density scales for the CBI and the OVRO 40 m are commensurate. The good agreement between the CBI and OVRO 40 m point source measurements is an important demonstration that both systems are working correctly.

The power and frequency spectra of fluctuations in our fields are extracted using a fit to the calibrated visibilities, after removal of the bright point sources. The CBI power spectrum measurements in Fig 1 (Padin et al. 2001a) are from a total of 150 hrs of observations of two main-trail pairs, one in the  $8^h$  CBI field and one in the  $14^h$  field. These observations were made with a ring configuration which did not have enough baselines in the 1–2 m range to allow us to break the degeneracy between the angular power spectrum and the frequency spectrum. Subsequent observations of the  $14^h$  field with a fairly compact array give a spectral index of  $\beta = 0.0 \pm 0.4$  at  $l \sim 600$ , so the signals we are measuring are consistent with black-body emission and any contamination from foregrounds is small. The initial results from the CBI are consistent with the  $\Omega_0 \sim 1$ ,  $\Omega_b h^2 \sim 0.02$ ,  $\Omega_\Lambda \sim 0.6$  models implied by

DASI (Halverson et al. 2001) and Boomerang (Netterfield et al. 2001) measurements at lower  $l$ .

## 9. CONCLUSIONS

The CBI has been making deep single-field observations and  $2^\circ \times 2^\circ$  mosaics for about a year. These observations should yield an accurate measurement of the power spectrum of CMBR fluctuations in the range  $500 < l < 2400$ , with an  $l$ -resolution of  $\sim 200$  (FWHM). Continuing deep-field observations and larger mosaics will provide measurements at higher  $l$ , and with improved  $l$ -resolution, allowing us to place strong constraints on the fundamental cosmological parameters.

During the first year of operation of the CBI we gained substantial experience working on complex equipment at the Chajnantor site. The biggest problem in this environment is the wind, and without the protection afforded by the dome we would not be able to maintain and operate the CBI. Lack of oxygen is also a serious problem, but portable oxygen systems have been very effective in enabling us to do strenuous and cognitive tasks. The site is excellent for CMBR observations when the weather is clear, but snow storms are frequent and access is often difficult. Pampa la Bola,  $\sim 10$  km to the east of the CBI, is more accessible in bad weather and, in retrospect, would have been a better choice.

In building the CBI we explored unconventional approaches for the mount and correlator. The CBI demonstrates that good pointing performance can be achieved with a compact, unbalanced mount, if corrections for the major structural deformations are applied. We use tilt-meters on the azimuth axis to measure deformations in the azimuth bearing and linear displacement transducers to measure deformations in the elevation shaft and encoder mount. The analog filterbank correlator used in the CBI is a departure from the current trend towards entirely digital processing in radio telescopes. The analog system has high efficiency and our wideband noise calibration scheme ensures that it is stable. It is very compact and fairly inexpensive and may be appropriate for other instruments which require wide bandwidth and high sensitivity.

This work was supported by the National Science Foundation (award AST-9802989), California Institute of Technology, Ronald and Maxine Linde and Cecil and Sally Drinkward.

## REFERENCES

AirSep Corp., Buffalo NY 14221, NewLife oxygen concentrator  
 American Space Frames Inc., Hernando FL 34442  
 APD Cryogenics Inc., Allentown PA 18103, model DE-204SL  
 refrigerator and model HC-8 compressor  
 Applied Geomechanics Inc., Santa Cruz CA 95062, model 701-1  
 Atlas Copco Chilena S.A.C., Iquique, Chile, model QAS 278  
 Ayers, W.P., 1957, IRE Trans. Microwave Theory Tech., 5(4), 258  
 BEI Precision Systems and Space Division, Little Rock, AR 72203,  
 model L695ERSDE  
 Brandt, W.N., Lawrence, C.R., Readhead, A.C.S., Pakianathan, J.N.  
 and Fiola, T.M., 1994, ApJ, 424, 21  
 Chad Therapeutics Inc., Chatsworth CA 91311, Oxymatic model 301  
 Clarricoats, P.J.B. and Olver, A.D., 1984, Corrugated Horns for  
 Microwave Antennas (London: Peregrinus) p. 153  
 Condon, J. J., et al., 1998, AJ, 115, 1693  
 Conway, R.G. and Kronberg, P.P., 1969, MNRAS, 142, 11  
 Cornwell, T.J., Holdaway, M.A. and Uson, J.M., 1993, A&A, 271,  
 697  
 Cudaback, D.D., 1984, PASP, 96, 463  
 Dawson, K.S., Holzapfel, W.L., Carlstrom, J.E., Joy, M., LaRoque,  
 S.J. and Reese, E.D., 2000, ApJ, submitted, astro-ph/0012151  
 Delta Tau Data Systems Inc., Northridge CA 91324, model PMAC-  
 VME  
 Gaustad, J.E., McCullough, P.R. and Van Buren, D., 1996, PASP,  
 108, 351  
 Gilbert, B., 1974, IEEE J. Solid-State Circuits, 9, 364  
 W. L. Gore Inc., Elkton MD 21922, fabric radome laminate RA7943  
 Halverson, N.W., et al., 2001, ApJ, submitted, astro-ph/0104489  
 Heidenhain Corp., Schaumburg IL 60173, model RCN 619  
 Hinshaw, G., et al., 1996, ApJ, 464, 17  
 Hu, W. and White, M., 1997, ApJ, 479, 568  
 Hu, W., Sugiyama, N. and Silk, J., 1997, Nature, 386, 37  
 Kildal, P-S., 1983, IEEE Trans. Antennas Propag., 31(6), 903

Kogut, A., 1999, in ASP Conf. Ser., Microwave Foregrounds, ed. A. de Oliveira-Costa and M. Tegmark (San Francisco: ASP) p. 91

Lay, O.P. and Halverson, N.W., 2000, ApJ, 543, 787

Leitch, E.M., Myers, S.T., Readhead, A.C.S. and Pearson, T.J., 1997, ApJ, 486, L23

Leitch, E.M., Readhead, A.C.S., Pearson, T.J., Myers, S.T., Gulkis, S. and Lawrence, C.R., 2000, ApJ, 532, 37

L & F Industries, Huntington Park CA 90255

Mather, J.C., 1981, IEEE Trans. Antennas Propag., 29(6), 967

Netterfield, C.B., et al., 2001, ApJ, submitted, astro-ph/0104460

Padin, S., Cartwright, J.K., Joy, M. and Meitzler, J.C., 2000, IEEE Trans. Antennas Propag., 48(5), 836

Padin, S., et al., 2001a, ApJ, 549, L1

Padin, S., Cartwright, J.K., Shepherd, M.C., Yamasaki, J.K. and Holzapfel, W.L., 2001b, IEEE Trans. Instrum. Meas., in press

Peacock, J.A., 1999, Cosmological Physics (Cambridge University Press) ch. 18

Peebles, P.J.E., 1993, Principles of Physical Cosmology (Princeton University Press) ch. 21

Pospieszalski, M.W., Nguyen, L.D., Lui, M., Liu, T., Thompson, M.A. and Delaney, M.J., 1994, IEEE MTT-S International Symposium Digest, 94.3, 1345

Pospieszalski, M.W., et al., 1995, IEEE MTT-S International Symposium Digest, 95.3, 1121

Readhead, A.C.S., Lawrence, C.R., Myers, S.T., Sargent, W.L.W., Hardebeck, H.E. and Moffet, A.T., 1989, ApJ, 346, 566

Rengelink, R.B., et al., 1997, A&A, 124, 259

RDP Electrosense, Pottstown PA 19465, model D5/10G8 LVDT and model SG-2.5 capacitive sensor

Seljak, U. and Zaldarriaga, M., 1996, ApJ, 469, 437

Seljak, U. and Zaldarriaga, M., 1997, CMBFAST (Cambridge: MIT)

Thompson, A.R. and D'Addario, L.R., 1982, Radio Sci., 17, 357

Thompson, A.R., Moran, J.M. and Swenson, G.W., 1986, Interferometry and Synthesis in Radio Astronomy (New York: Wiley) ch. 6

Urry, W.L., Thornton, D.D. and Hudson, J.A., 1985, PASP, 97, 745

Webster, A., 1994, MNRAS, 268, 299

West, J.B., 1995, Respiration Physiology, 99, 225

Wind River Systems Inc., Alameda CA 94501

Zaldarriaga, M., Seljak, U. and Bertschinger, E., 1998, ApJ, 494, 491